Article

Revisiting Pt foil catalysts for formamide electrosynthesis achieved at industrial-level current densities

Xinzhong Wang [1,7], Yiwen Su[1,7], Jiashu Chen [1,7], Edward Hengzhou Yan[2], Qing Xia[1], Jie Wu [1], Shanhe Gong[1], Mingcong Tang[1], Wai Sze Yip[2], Yongbiao Mu[3], Yuyang Yi[2], Jinjin Wu[1], Fujing Xu[1], Xianzhong Yang[4], Xiao Zhang [1] ✉, Shixue Dou[4,5] ✉, Jingyu Sun [6] ✉ & Guangping Zheng [1] ✉

Current electrosynthesis catalysts typically rely on nanomaterial-based engineering with multi-dimensional structural modifications. However, such approaches may not always be necessary, especially for underexplored industrial electrochemical conversions. Here, we demonstrate that commercial platinum (Pt) foil catalysts excel in the electrochemical co-oxidation of waste polyethylene terephthalate (PET)-derived ethylene glycol (EG) and ammonia (NH_3) into formamide ($HCONH_2$), a process traditionally reliant on energy-intensive methods. This approach achieves a high Faradaic efficiency (FE) of $55.87 \pm 1.4\%$ and a productivity of 1003.63 ± 23.72 μmol cm^{-2} h^{-1} at industrially relevant current densities without any degradation for durable operation (more than 500 h and 300 h for H-cell and membrane electrode assembly (MEA) reactor, respectively). In situ spectroscopy, supported by theoretical calculations, suggests that $*CH_2O$ and $*NH_2$ are likely key intermediates. Furthermore, the product sustainability index (ProdSI) and techno-economic analysis (TEA) underscore the cost-effectiveness and sustainability of noble Pt foil in this scenario, challenging the conventional reliance on complex electrocatalysts. This work provides distinctive insights into catalyst screening and demonstrates a viable strategy for upcycling waste plastics.

Renewable electrochemical conversion protocols are emerging with strong potential as an alternative to energy-intensive industrial chemical reactions[1-5]. Attributed to controllable rate and pathways of electrochemical reactions, waste resources can be converted into value-added products with reduced carbon footprint (Fig. 1a)[6-10]. Catalysts, as the engines for electrosynthesis, attract much attention

from researchers, and enormous efforts have been put into downscaling the dimensions of catalysts for increased specific area[11-15]. Hence, catalyst nano-engineering is deemed as the holy grail in most recently developed electrocatalysis systems[16,17]. Nevertheless, latent uncertainty regarding the stability and cost-effectiveness exists behind the prosperity in catalyst nano-engineering. Attributed to aggregation

[1]Department of Mechanical Engineering, The Hong Kong Polytechnic University, Hung Hom, Kowloon, Hong Kong, China. [2]Research Institute for Advanced Manufacturing, Hong Kong Polytechnic University, Kowloon, Hong Kong, China. [3]Department of Mechanical and Energy Engineering, Southern University of Science and Technology, Shenzhen, China. [4]Institute of Energy Materials Science, University of Shanghai for Science and Technology, Shanghai, China. [5]Institute for Superconducting and Electronic Materials, University of Wollongong, Innovation Campus, Squires Way, North Wollongong, New South Wales, Australia. [6]Soochow Institute for Energy and Materials Innovations, Key Laboratory of Advanced Carbon Materials and Wearable Energy Technologies of Jiangsu Province, Soochow University, Suzhou, China. [7]These authors contributed equally: Xinzhong Wang, Yiwen Su, Jiashu Chen. ✉e-mail: xiao1.zhang@polyu.edu.hk; shi@usst.edu.cn; sunjy86@suda.edu.cn; mmzheng@polyu.edu.hk
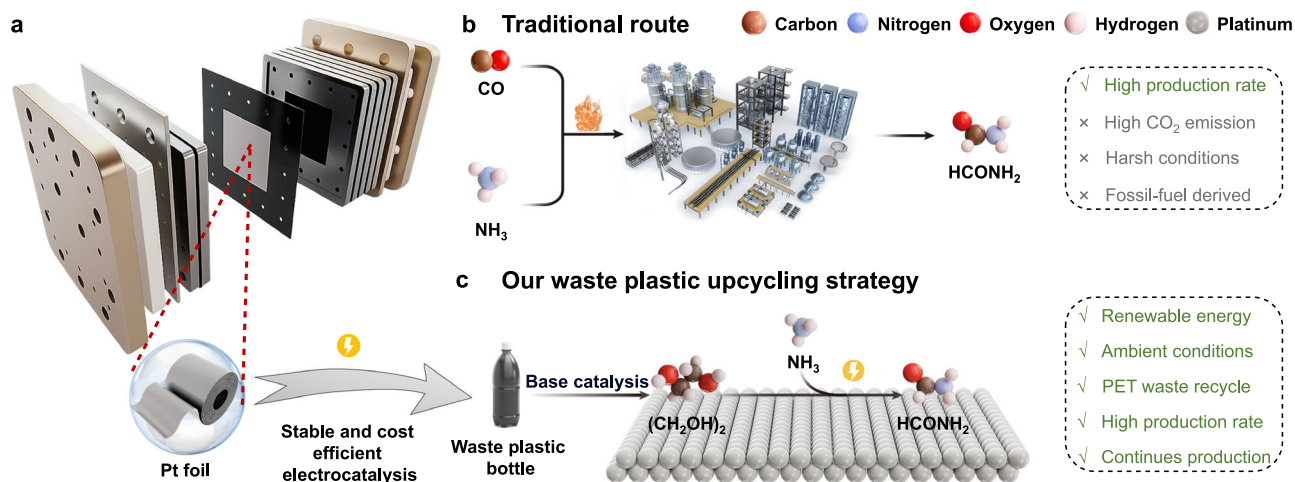
Fig. 1 | Strategies for HCONH$_2$ synthesis. Schematic of (**a**) an integrating clean energy for sustainable production. **b** The traditional route, and (**c**) our plastic waste upcycling strategy for HCONH$_2$ synthesis.

of nanoparticles (resulting from weakened selectivity, Ostwald ripening, etc.), structure transformation, corrosion, unstable substrate, and many other unexpected factors[18–20], nano-catalyst stability can hardly be ensured, especially for industrial-scale electrosynthesis[21,22]. More importantly, the lack of quantitative analysis makes the cost-effective comparison between non-noble metal catalysts and noble-metal counterparts ambiguous.

Herein, as a proof of concept, we systematically investigate the performance of non-noble metal nanocatalysts and mature noble metal electrodes during electrochemical synthesis with the production of formamide (HCONH$_2$) as the representative. Traditionally, HCONH$_2$ is produced industrially through the reaction of carbon monoxide (CO) and ammonia (NH$_3$) under high temperature and pressure (Fig. 1b), which is energy-intensive and results in tremendous emissions of greenhouse gases[23,24]. Thus, electro/photocatalytic synthesis of HCONH$_2$ becomes a promising solution to tackle the aforementioned challenges[25–31]. Studies have yielded a favorable Faradaic efficiency (FE) of 40.39% and a productivity of 515 μmol cm^{-2} h^{-1} through electrochemical upgrading of methanol (CH$_3$OH) to HCONH$_2$ via coupled NH$_3$ co-oxidation over platinum (Pt)-based catalysts under ambient conditions. (Supplementary Fig. 1)[29], but the high cost of CH$_3$OH makes this method impractical. Others, like electrochemical upgrading of ethylene glycol (EG, (CH$_2$OH)$_2$) to HCONH$_2$, is handicapped with side reactions like the formation of ammonium sulfate ((NH$_4$)$_2$SO$_4$), and the unfavorable stability[32].

In contrast, we focus on commercial catalysts, harnessing mature preparation and employment cases, and facilitating the implementation of the electrochemical reaction that has not been well investigated. Among them, Pt foil is chosen based on its advantageous adsorption/desorption energies, and EG from plastic degradation coupled with NH$_3$ in potassium bicarbonate (KHCO$_3$) solution is chosen as the sample electrosynthesis processes (Fig. 1c)[33]. Thereinto, by avoiding (NH$_4$)$_2$SO$_4$ through the application of a weakly alkaline environment, the system achieves an FE of $55.87 \pm 1.4\%$ and a productivity of 694.9 ± 17.46 μmol cm^{-2} h^{-1} at industrially relevant current densities without any degradation for durable operation (> 500 h) in an H-type cell[34–37]. A production rate of 1003.63 ± 23.72 μmol cm^{-2} h^{-1} is obtained at a current density of 150 mA cm^{-2}, which is double that of reported systems[32]. For the practical membrane electrode assembly (MEA) reactor configuration, the FE still consistently exceeds 40% with stable cycling at 100 mA cm^{-2} for more than 300 h. Mechanistic studies using in situ attenuated total reflectance surface-enhanced infrared absorption

spectroscopy (ATR-SEIRAS), in situ differential electrochemical mass spectrometry (DEMS), and supported by density functional theory (DFT) calculations suggest that *CH$_2$O and *NH$_2$ are likely key electrophilic intermediates involved in the formation of HCONH$_2$. Product sustainability index (ProdSI) and techno-economic analysis (TEA) further highlight the high cost-effectiveness and strong sustainability for noble Pt foil catalysts, which is opposite to the common perception of the selection of electrocatalysts. This study adds one dimension for future catalyst design and selection, and also paves the way for underlying electrochemical conversions originating from energy-intensive industrial reactions.

Results

Initial evaluation for the electrochemical synthesis of HCONH$_2$

The electrochemical synthesis of HCONH$_2$ is initially explored in an H-type cell equipped with a proton exchange membrane (PEM, Supplementary Fig. 2). The adopted electrolyte is 10.0 mL, affording 4.0 M EG, 1.0 M NH$_3$, and 0.5 M KHCO$_3$. EG and NH$_3$ are chosen as C and N sources, respectively, while KHCO$_3$ serves to stabilize pH, improve ionic conductivity, and suppress the formation of formic acid (HCOOH). A commercial Pt foil is employed as the cathode to facilitate the hydrogen evolution reaction (HER). Ten commercial anode catalysts—PtRu/C, Pt/C, Pt foil, Pd foil, TiO$_2$, Ni(OH)$_2$, NiO, Co$_3$O$_4$, MoS$_2$, and Ag—each with an active area of 1.0 cm^2, are systematically evaluated using galvanostatic methods. The carbonaceous liquid products are analyzed and quantified via ^{1}H-nuclear magnetic resonance (^{1}H-NMR, Supplementary Fig. 3).

Electrolysis experiments are conducted at current densities of 20, 50, and 100 mA cm^{-2} for durations of 5 h, 2 h, and 1 h, respectively (Supplementary Figs. 4–6 and Fig. 2a). Among the catalysts evaluated, Pt foil showed favorable performance for HCONH$_2$ production, achieving FE of 34.54%, 44.71%, and 56.86% under the conditions mentioned above. To validate the experimental results, DFT calculations are performed to evaluate the adsorption energies (E$_{ads}$) of EG, NH$_3$, and HCONH$_2$ on various catalyst surfaces[38]. Accurate theoretical modeling necessitated the identification of the active catalyst phase during the reaction. Operando Raman spectroscopy is performed on all commercial catalysts under a constant current density of 50 mA cm^{-2}, with spectra collected at 0 s, 30 s, 1 min, 2 min, 5 min, 8 min, and 10 min. The results revealed that most catalysts experienced varying degrees of surface reconstruction under anodic conditions. These observations are used to guide the selection of representative surface models for DFT calculations.
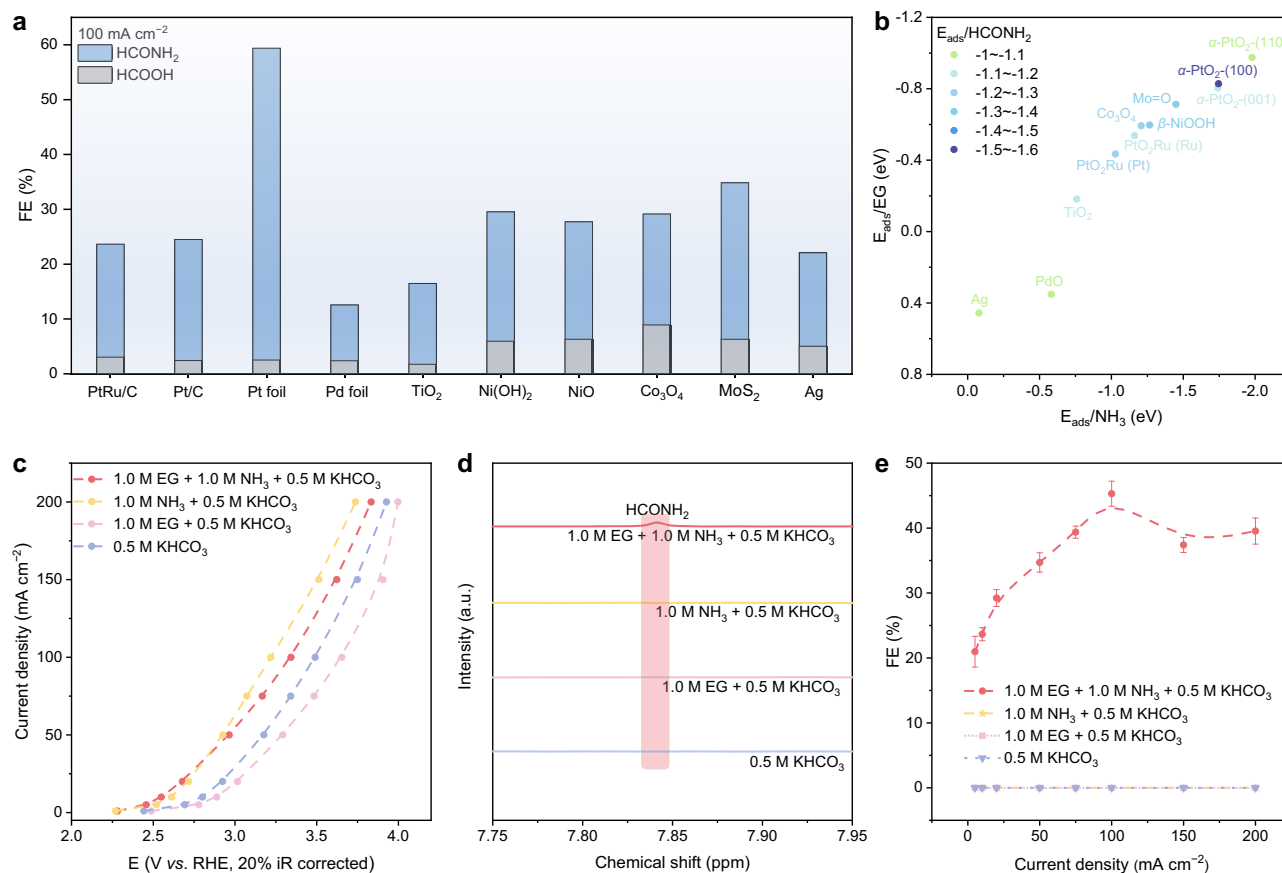
Fig. 2 | Initial evaluation of catalysts and conditions for electrochemical HCONH$_2$ synthesis. a Catalysts screening of HCONH$_2$ electrosynthesis after 1 h at 100 mA cm^{-2} based on galvanostatic methods (4.0 M EG + 1.0 M NH$_3$ + 0.5 M KHCO$_3$. pH: 9.44 ± 0.032). **b** E$_{ads}$ of EG, NH$_3$, and HCONH$_2$ on various catalyst surfaces. **c** I–V curves (with 20% iR compensation versus RHE) under varying conditions (1.0 M EG + 1.0 M NH$_3$ + 0.5 M KHCO$_3$, 1.0 M NH$_3$ + 0.5 M KHCO$_3$, 1.0 M EG + 0.5 M KHCO$_3$, and 0.5 M KHCO$_3$. pH: 10.00 ± 0.030, 10.00 ± 0.040, 8.30 ± 0.012, and 8.00 ± 0.028; Resistance: 5.47 ± 0.332, 4.63 ± 0.189, 7.86 ± 0.269, and 6.17 ± 0.435 ohms). **d** ^{1}H NMR spectra after 1 h of continuous electrolysis at 100 mA cm^{-2} under the four conditions. **e** FEs of HCONH$_2$ under each condition. The error bars represent the standard deviation of three independent measurements. Source data are provided as a Source Data file.

In particular, Pt-based systems (PtRu/C, Pt/C, and Pt foil; Supplementary Fig. 7a–c) exhibited a characteristic band at ~531–543 cm^{-1}, attributed to α-PtO$_2$, confirming the oxidative surface reconstruction[29,39,40]. However, to rule out possible contributions from other Pt oxides such as β-PtO$_2$, we further conducted X-ray photoelectron spectroscopy (XPS) and X-ray diffraction (XRD) analyses. The high-resolution XPS analysis for the Pt foil after electrolysis (Supplementary Fig. 8a) revealed a peak at ~79.6 eV, confirming the presence of oxidized Pt^{4+} $4f_{5/2}$ species[41]. Yet due to the nearly identical binding energies of α- and β-PtO$_2$, XPS alone cannot discriminate between the two phases. Therefore, XRD is performed to determine the crystal structure: the pristine Pt foil displayed sharp reflections consistent with metallic Pt (PDF#04-0802), whereas the post-electrolysis sample showed additional peaks matching well with α-PtO$_2$ (PDF#37-1087), with no signals assignable to β-PtO$_2$ (Supplementary Fig. 8b, c). These results collectively confirm that α-PtO$_2$ is the dominant surface oxide phase formed during electrolysis.

Additional Ru–O signals (~485 cm^{-1}) observed in PtRu/C further support dual-metal surface evolution[39]. Pd foil (Supplementary Fig. 7d) exhibited bands at ~483 and ~528 cm^{-1}, corresponding to PdO formation[42]. Ni(OH)$_2$ and NiO (Supplementary Fig. 7f, g) showed bands at ~504 cm^{-1}, indicative of β-NiOOH formation[29,43,44]. MoS$_2$ (Supplementary Fig. 7i) displayed a distinct band at ~864 cm^{-1}, assigned to Mo=O stretching vibrations, suggesting surface oxidation[45]. These reconstructed states are adopted for subsequent E$_{ads}$ analyses. In contrast, TiO$_2$ (Supplementary Fig. 7e), Co$_3$O$_4$ (Supplementary Fig. 7h),

and Ag (Supplementary Fig. 7j) exhibited no noticeable spectral changes, suggesting structural stability under the reaction conditions[44,46,47]. These operando insights provided an experimental basis for rational catalyst model construction in the theoretical calculations.

In Fig. 2b, the horizontal and vertical axes represent the E$_{ads}$ of NH$_3$ and EG on various catalyst surfaces, respectively. The color intensity indicates the E$_{ads}$ of HCONH$_2$, while the adsorption configurations are illustrated in Supplementary Fig. 9. Notably, α-PtO$_2$-(110) crystal plane demonstrates the lower E$_{ads}$ for NH$_3$ and EG, which are conducive to their adsorption for subsequent reactions. Simultaneously, this crystallography plane shows favorable E$_{ads}$ for HCONH$_2$, facilitating its surfacial desorption while preventing product accumulation on active sites. Similarly, other crystal planes of α-PtO$_2$, such as (100) and (001) planes, along with MoS$_2$ and Ni(OH)$_2$ catalysts, exhibit low E$_{ads}$ for NH$_3$ and EG and high E$_{ads}$ for HCONH$_2$, validating their catalytic efficacy in converting EG to HCONH$_2$. These findings align well with electrochemical screening, demonstrating the feasibility of Pt foil in HCONH$_2$ formation, which affords in situ surfacial conversion.

To elucidate the roles of C and N sources in the formation of HCONH$_2$, current-voltage (I–V) curves (with 20% iR compensation versus RHE) and solution resistance are measured using various electrolyte compositions in 0.5 M KHCO$_3$ (Fig. 2c and Supplementary Fig. 10). In the presence of 1.0 M NH$_3$ (without EG), the onset potential is lower. The addition of 1.0 M EG increases the voltage significantly at a current density above 50 mA cm^{-2}[48–50]. Conversely, the presence of
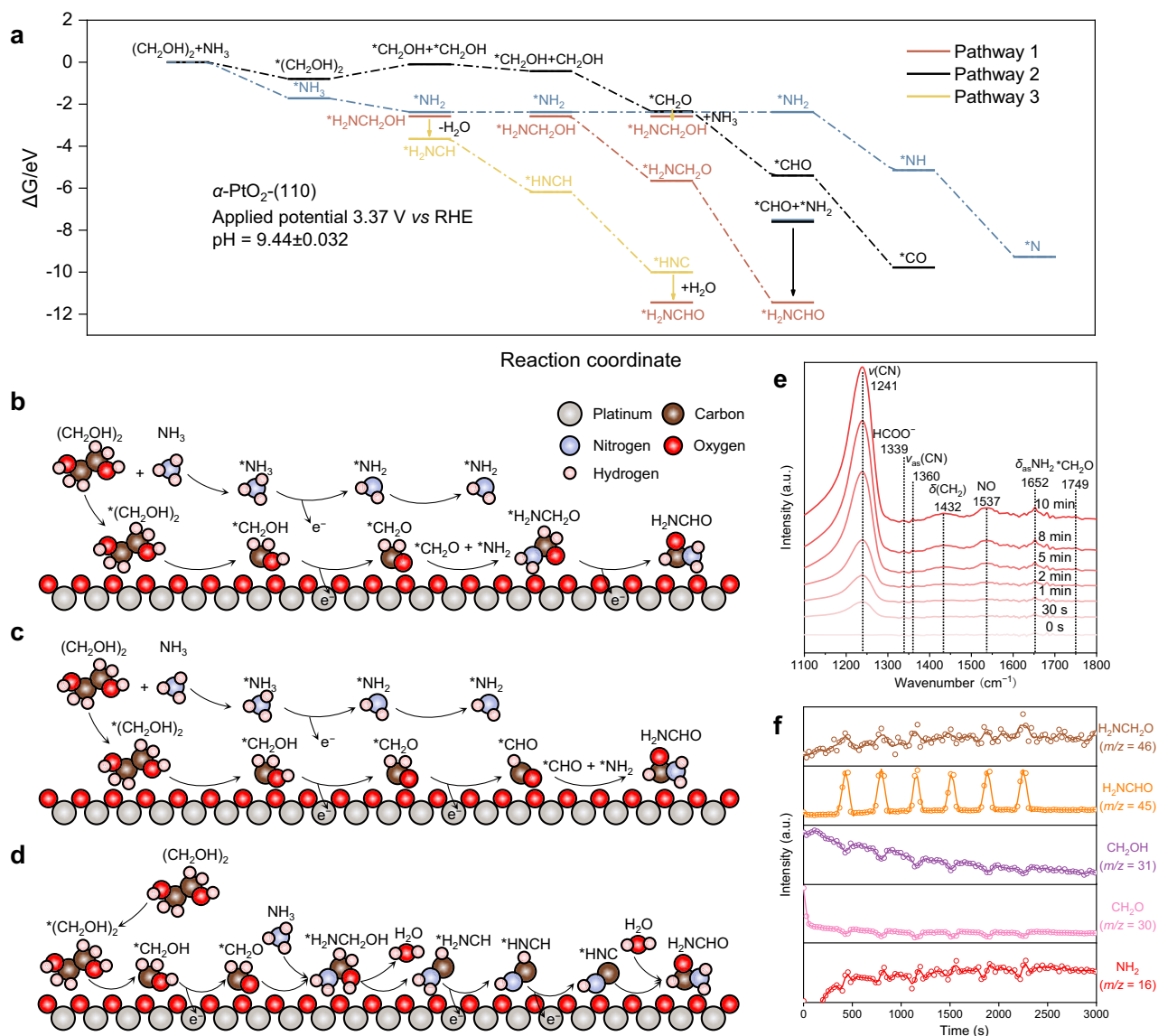
Fig. 3 | Mechanistic investigation of HCONH$_2$ electrosynthesis. a Free energy diagrams for proposed reaction pathways on α-PtO$_2$-(110). **b–d** Schematic diagram of pathway 1, 2, and 3 for HCONH$_2$ synthesis during the co-oxidation of EG and NH$_3$ over the surface of α-PtO$_2$-(110). **e** In situ ATR-SEIRAS spectra during the reaction for the formation of HCONH$_2$ in 4.0 M EG + 1.0 M NH$_3$ + 0.5 M KHCO$_3$ electrolyte over Pt foil catalyst. **f** In situ DEMS signals for m/z = 46 (H$_2$NCH$_2$O), 45 (H$_2$NCHO), 30 (CH$_2$O), and 16 (NH$_2$) species. Source data are provided as a Source Data file.

1.0 M EG (without NH$_3$) leads to a higher onset potential and voltage compared to the case with 0.5 M KHCO$_3$ alone. The results suggest that NH$_3$ oxidation is energetically favorable and occurs prior to EG oxidation, harnessing a higher decomposition energy barrier[51–53]. ^{1}H NMR spectra confirm the sole formation of HCONH$_2$ when both EG and NH$_3$ are presented (Fig. 2d). At varying current densities (5–200 mA cm^{-2}), an FE of 45.29 ± 1.93% is observed at 100 mA cm^{-2}, along with a production rate of 563.3 ± 24.05 μmol cm^{-2} h^{-1} (Fig. 2e). At 200 mA cm^{-2}, the FE can be maintained at 39.54 ± 2.02%, with a production rate of 983.56 ± 50.16 μmol cm^{-2} h^{-1} (Supplementary Fig. 11).

Investigation on the reaction mechanism for electrochemical HCONH$_2$ synthesis

Identifying key intermediates is essential to the understanding of mechanisms for the electrosynthesis of HCONH$_2$ from EG. The analysis of substantial reaction pathways is conducive to the optimization of reaction conditions and the extension of the electrochemical methodology to other applications, such as waste treatment. To this end, four high-performing catalysts: Pt foil, Pt/C, MoS$_2$, and Ni(OH)$_2$ are selected

from the initial screening of ten materials. DFT calculations are performed to explore the reaction pathways on three crystal planes ((110), (100), and (001) planes) of α-PtO$_2$, β-Ni(OH)$_2$, and 1T-MoS$_2$ (Fig. 3a and Supplementary Figs. 12–15), and the configurations are illustrated in Supplementary Data 1. The reaction begins with the oxidation of NH$_3$ to form the *NH$_2$ intermediate, which is consistent with the experimental result as shown in Fig. 2c. Simultaneously, EG interacts with the catalyst surface, that the system energy is reduced, indicating the stability of such a process. Subsequently, the cleavage of the C–C bond in EG generates two hydroxymethyl (*CH$_2$OH) fragments, causing a moderate increase in free energy, which is consistent with reported results[54]. The pathway is observed for all four catalysts, with free energy changes (ΔG) calculated to be 0.70 eV, 1.38 eV, 1.98 eV, 2.10 eV, and 1.21 eV for α-PtO$_2$-(110), -(100), and -(001), β-Ni(OH)$_2$, and 1T-MoS$_2$, respectively. Notably, α-PtO$_2$-(110) exhibits the lower ΔG, indicating that it is more reactive and has superior catalytic performance, which is consistent with the results shown in Fig. 2b.

Subsequent analyses on the formation of HCONH$_2$ on α-PtO$_2$-(110) are carried out, with three primary pathways proposed (Fig. 3a and

Supplementary Fig. 16). In the reaction coordinate diagram, the vertical axis represents free energy changes, while the horizontal axis denotes the reaction progress. The desorption of *CH$_2$OH results in a significant free energy decrease (− 0.32 eV), followed by its partial oxidation in generating the aldehyde intermediate *CH$_2$O, which induces a modest decrease in free energy (− 1.92 eV). Pathway 1 (red dashed line) involves the reaction between *CH$_2$O and NH$_3$-derived intermediate *NH$_2$, which produces hemiaminal (*H$_2$NCH$_2$O) as accompanied by a decrease in free energy to − 5.65 eV. This intermediate undergoes further dehydrogenation that yields HCONH$_2$, with the system's free energy decreased to − 11.44 eV (Fig. 3b)[55]; Pathway 2 (black dashed line) involves the subsequent dehydrogenation of *CH$_2$O to *CHO, which then couples with *NH$_2$ to form HCONH$_2$ (Fig. 3c); Pathway 3 (yellow dashed line) indicates that *CH$_2$O could react directly with NH$_3$ to form *H$_2$NCH$_2$OH. This intermediate is hydrolyzed to *H$_2$NCH, which subsequently undergoes two dehydrogenation steps, yielding the nitrile intermediate *HNC and ultimately HCONH$_2$ (Fig. 3d)[56]. Among these pathways, the crucial dehydration step of *NH$_2$CH$_2$OH is thermodynamically viable only over α-PtO$_2$, with Gibbs free energy of − 1.08 eV. The results suggest that α-PtO$_2$ facilitates HCONH$_2$ formation predominantly by going through pathway 1, where pathway 3 is an alternative.

In contrast, pathway 2 involves the C−N coupling of two adjacent reactive intermediates, *CHO and *NH$_2$, both of which are prone to oxidation, leading to the formation of C/N-containing by-products[57]. Consequently, the direct nucleophilic attack of NH$_3$ on the in situ formed aldehyde *CH$_2$O, as proposed in pathways 1 and 3, appears to be more feasible. During the formation of the *CHO intermediate in pathway 2, the system undergoes a free energy decrease of − 3.06 eV, resulting in a total free energy of − 5.4 eV. Upon the formation of HCONH$_2$, the coupling of *CHO and *NH$_2$ leads to a further energy reduction to − 7.6 eV, with an energy change of − 3.84 eV. Comparatively, the energy change from *NH$_2$CH$_2$O to HCONH$_2$ in pathway 1 is − 5.79 eV, while the transition from *HNC to HCONH$_2$ in pathway 3 involves the energy change of − 1.44 eV. These findings underscore that among the three reaction pathways for producing HCONH$_2$ from EG, pathway 1 is the most energetically favorable and thus becomes the primary route.

To elucidate the mechanistic pathway for HCONH$_2$ formation, in situ ATR-SEIRAS is employed to monitor the real-time evolution of reaction intermediates and ionic species at the catalyst-electrolyte interface. Measurements are conducted in an electrolyte comprising 0.5 M KHCO$_3$, 4.0 M EG, and 1.0 M NH$_3$ under galvanostatic conditions at a current density of 50 mA cm^{-2}. Spectra are recorded at time intervals of 0 s, 30 s, 1 min, 2 min, 5 min, 8 min, and 10 min (Fig. 3e). The time-dependent growth of multiple infrared bands revealed the stepwise formation and accumulation of adsorbed intermediates on the catalyst surface.

According to established vibrational assignments, the band at 1241 cm^{-1} corresponds to the C−N stretching vibration of HCONH$_2$. Additional bands at 1339 and 1360 cm^{-1} correspond to formate (HCOO$^-$) and the asymmetric C−N stretching mode of HCONH$_2$, respectively. The peak at 1652 cm^{-1} is assigned to the asymmetric bending vibration (δ_{as}NH$_2$) of adsorbed *NH$_2$ as well as the N−H bending in HCONH$_2$. A strong feature at ~1745 cm^{-1} is indicative of *CH$_2$O species, consistent with earlier reports. To ensure the fidelity of these assignments, reference IR spectra are acquired for a set of standard compounds, including HCONH$_2$, HCOOH, EG, NH$_3$, KHCO$_3$, and K$_2$CO$_3$ (Supplementary Fig. 17), showing good agreement with the in situ data and supporting the molecular origins of the observed features[28,32,58−62].

To further corroborate these findings, in situ DEMS is conducted under alternating potentials. The detection of mass-to-charge (m/z) signals at 46 (H$_2$NCH$_2$O), 45 (H$_2$NCHO), 30 (CH$_2$O), and 16 (NH$_2$) provided direct evidence of key reactive intermediates and final products

(Fig. 3f). These mass fragments align with the infrared bands at 1241, 1360, 1652 and 1749 cm^{-1}, respectively, supporting a mechanistic pathway involving the coupling of *CH$_2$O and *NH$_2$ in the formation of HCONH$_2$. Taken together, DFT calculations and spectroscopic measurements suggest that pathway 1 on the α-PtO$_2$-(110) surface is likely involved in the electrocatalytic synthesis of HCONH$_2$.

Optimization of electrochemical performance for HCONH$_2$ synthesis

To elucidate the effect of reactant concentration on reactivity, initial tests with various concentrations of EG are conducted. As the EG concentration increases, both current density and resistance increase, likely due to the formation of more active electrophilic intermediates through EG oxidation (Fig. 4a and Supplementary Figs. 18, 19). With the increases in EG concentration from 1.0 M to 8.0 M, the FE of HCONH$_2$ initially increases and then decreases (Fig. 4b, and Supplementary Fig. 20). In contrast, the FE of HCOOH increases with increasing EG concentration (Supplementary Fig. 21). The conversion ratio remains stable with all concentrations (Supplementary Fig. 22). At 100 mA cm^{-2}, the FE for HCONH$_2$ is 55.87 ± 1.4% with an EG concentration of 4.0 M. At 150 mA cm^{-2}, using 4.0 M EG, the FE remains at 53.8 ± 1.27%, with a production rate of 1003.63 ± 23.72 µmol cm^{-2} h^{-1} (Fig. 4c). The NH$_3$ concentration also influences product selectivity, with an FE of 55.87 ± 1.4% observed at 1.0 M NH$_3$ (Supplementary Fig. 23).

In addition, the impact of electrolyte composition on reaction reactivity is examined using various electrolytes. The I−V curves (with 20% iR compensation versus RHE) and resistances of a solution containing 4.0 M EG and 1.0 M NH$_3$ are measured in the electrolytes of 0.5 M potassium hydroxide (KOH), 0.5 M KHCO$_3$, 0.25 M sulfuric acid (H$_2$SO$_4$) and 0.25 M potassium sulfate (K$_2$SO$_4$) (Fig. 4d and Supplementary Fig. 24), ensuring a consistent number of cations. The reaction demonstrates the low onset potential in a 0.5 M KHCO$_3$ solution. In the 0.5 M KOH solution, a lower voltage is observed at the same current density after 20 mA cm^{-2} as compared to that in the 0.5 M KHCO$_3$ solution. At this stage, the only carbonaceous liquid product is HCOOH, with HCONH$_2$ being completely suppressed in the 0.5 M KOH solution (Supplementary Fig. 25). Such suppression may result from the reaction between the intermediate *CHO resulting from EG oxidation and OH$^-$, producing HCOOH[63,64]. Upon reducing the alkalinity, the production of HCONH$_2$ can be observed, further supporting the hypothesis regarding the reaction. In the 0.25 M H$_2$SO$_4$ electrolyte, the yield of HCONH$_2$ is slightly higher than that in 0.5 M KOH, but remains significantly lower than that in KHCO$_3$. The result supports the hypothesis that acidic conditions protonate NH$_3$ into NH$_4^+$, thereby reducing its nucleophilicity and promoting the formation of byproducts such as (NH$_4$)$_2$SO$_4$, which hinder C−N coupling[65,66]. In contrast, KHCO$_3$ provides a weakly alkaline buffering environment that suppresses undesired ammonium salt formation and facilitates selective *NH$_2$−*CH$_2$O coupling toward HCONH$_2$. At various current densities (5−200 mA cm^{-2}), the FE of HCONH$_2$ in 0.5 M KHCO$_3$ electrolyte reaches 55.87 ± 1.4% at 100 mA cm^{-2}, which is comparatively higher than under other conditions (Fig. 4e). At 150 mA cm^{-2}, the conversion ratio remains approximately 90%, and the FE reaches 53.8 ± 1.27%, corresponding to a production rate of 1003.63 ± 23.72 µmol cm^{-2} h^{-1} (Supplementary Figs. 26, 27).

To evaluate thermal effects, the FE for the system with 4.0 M EG + 1.0 M NH$_3$ + 0.5 M KHCO$_3$ is tested at various temperatures (20−60 °C) at 100 mA cm^{-2}. The FE observed under laboratory conditions at room temperature (20 °C) is relatively higher (Supplementary Fig. 28). Under these conditions (4.0 M EG + 1.0 M NH$_3$ + 0.5 M KHCO$_3$ at 20 °C), we quantified FEs for all detectable products: HCONH$_2$, HCOOH, NO$_2$, NO, N$_2$, CO$_2$, CO, and O$_2$ over 5−200 mA cm^{-2}. Across this current-density range, HCONH$_2$ is the dominant carbonaceous product, oxygen evolution reaction (OER) is the main competing pathway, producing O$_2$ as the principal by-product, its FE is 15.37% at
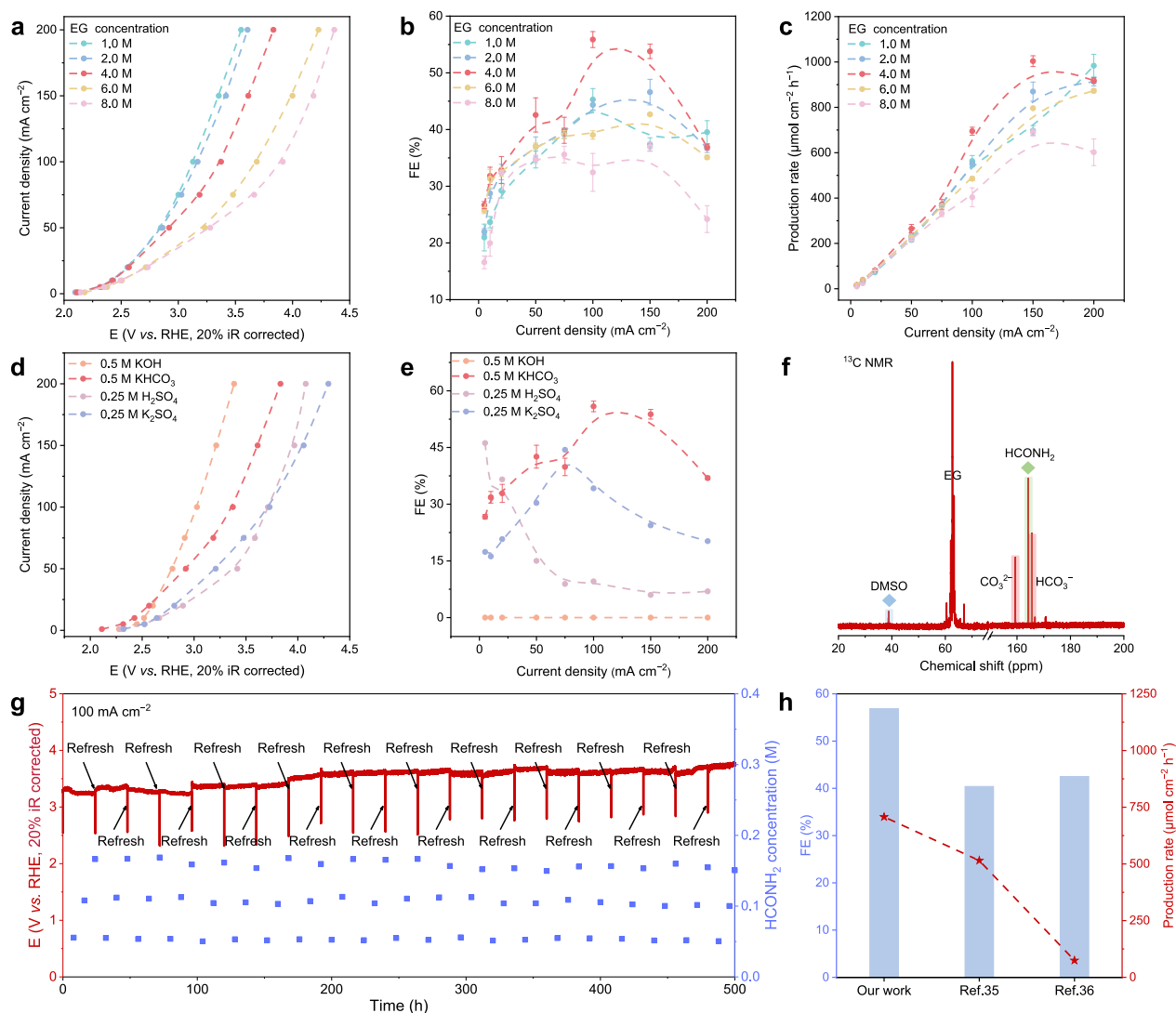
Fig. 4 | Optimization of the EG and NH₃ co-oxidation system. a I–V curves (with 20% iR compensation versus RHE), (**b**) FEs, and (**c**) production rates with varying EG concentrations (1.0–8.0 M) in 1.0 M NH_3 + 0.5 M $KHCO_3$ (pH: 9.38 ± 0.016, 9.52 ± 0.029, 9.44 ± 0.032, 9.54 ± 0.035, and 9.52 ± 0.012; Resistance: 5.235 ± 0.151, 5.235 ± 0.491, 8.416 ± 0.264, 12.20 ± 0.02, and 15.219 ± 0.287 ohms). **d** I–V curves (with 20% iR compensation versus RHE), and (**e**) FEs in 4.0 M EG + 1.0 M NH_3 with different electrolytes (0.5 M KOH, 0.5 M $KHCO_3$, 0.25 M H_2SO_4, and 0.25 M K_2SO_4 (pH: 12.51 ± 0.045, 9.44 ± 0.032, 9.58 ± 0.017, 11.17 ± 0.048; Resistance: 4.62 ± 0.24, 8.416 ± 0.264, 8.03 ± 0.301,

and 11.173 ± 0.442 ohms) (**f**) ^{13}C NMR spectra for the electrolyte solution of 4.0 M EG + 1.0 M NH_3 + 0.5 M $KHCO_3$ after 1 h at 100 mA cm^{-2}. **g** Chronopotentiometry experiment profile showing the cell voltage (with 20% iR compensation versus RHE) and $HCONH_2$ production at 100 mA cm^{-2} over 500 h in an H-type cell (4.0 M EG + 1.0 M NH_3 + 0.5 M $KHCO_3$, electrolyte refreshed every 24 h. pH: 9.44 ± 0.032; Resistance: 8.416 ± 0.264 ohms). **h** Comparison on the performance against those reported H-type cell systems. The error bars in (**b**), (**c**), and (**e**) represent the standard deviation of three independent measurements. Source data are provided as a Source Data file.

100 mA cm^{-2}, and all other products appear only in minor amounts (Supplementary Fig. 29). The formation of $HCONH_2$ is further confirmed by a distinct signal at 164.2 ppm in the ^{13}C NMR spectra (Fig. 4f). The stability of the H-cell for $HCONH_2$ electrosynthesis is tested in a solution of 4.0 M EG + 1.0 M NH_3 + 0.5 M $KHCO_3$ at 100 mA cm^{-2}. The cell voltage and $HCONH_2$ production rate remain stable for over 500 hours, with the electrolyte refreshed every 24 hours (Fig. 4g). After cycling, the extent of O_2 increases on the Pt foil, suggesting the occurrence of self-activation in the electrosynthesis process (Supplementary Fig. 30). It is also worth noting that no Pt would be consumed except for the self-activation surficial reaction. This system demonstrates superior performance compared to other reported electrochemical methods for $HCONH_2$ production (Fig. 4h)[29,32]. In terms of product selectivity, the electrosynthesis system achieves a higher FE of 55.87 ± 1.4% at an industrial-level current density of 100 mA cm^{-2}. The production rate of 1003.63 ± 23.72 μmol cm^{-2} h^{-1} with a high FE of

53.8 ± 1.27% is double the reported values, which is obtained at 150 mA cm^{-2}. Additional comparisons in Supplementary Table 1 highlight substantial improvements in key performance metrics, underscoring the advantages of this electrosynthesis strategy.

Continuous production of $HCONH_2$ in a membrane electrode assembly reactor

To achieve continuous production of $HCONH_2$, an MEA reactor is developed to replace the traditional H-type cell used in the electrosynthesis (Supplementary Fig. 31). In this setup, titanium plates act as anode current collectors, while stainless steel plates serve as cathode current collectors. Commercial Pt foils (1.0 cm × 1.0 cm) are used as catalysts at both the anode and cathode, taking advantage of their high catalytic activity and stability. Based on the optimized conditions, the anolyte consists of a solution of 4.0 M EG + 1.0 M NH_3 + 0.5 M $KHCO_3$, with H_2O acting as the catholyte. The anode and
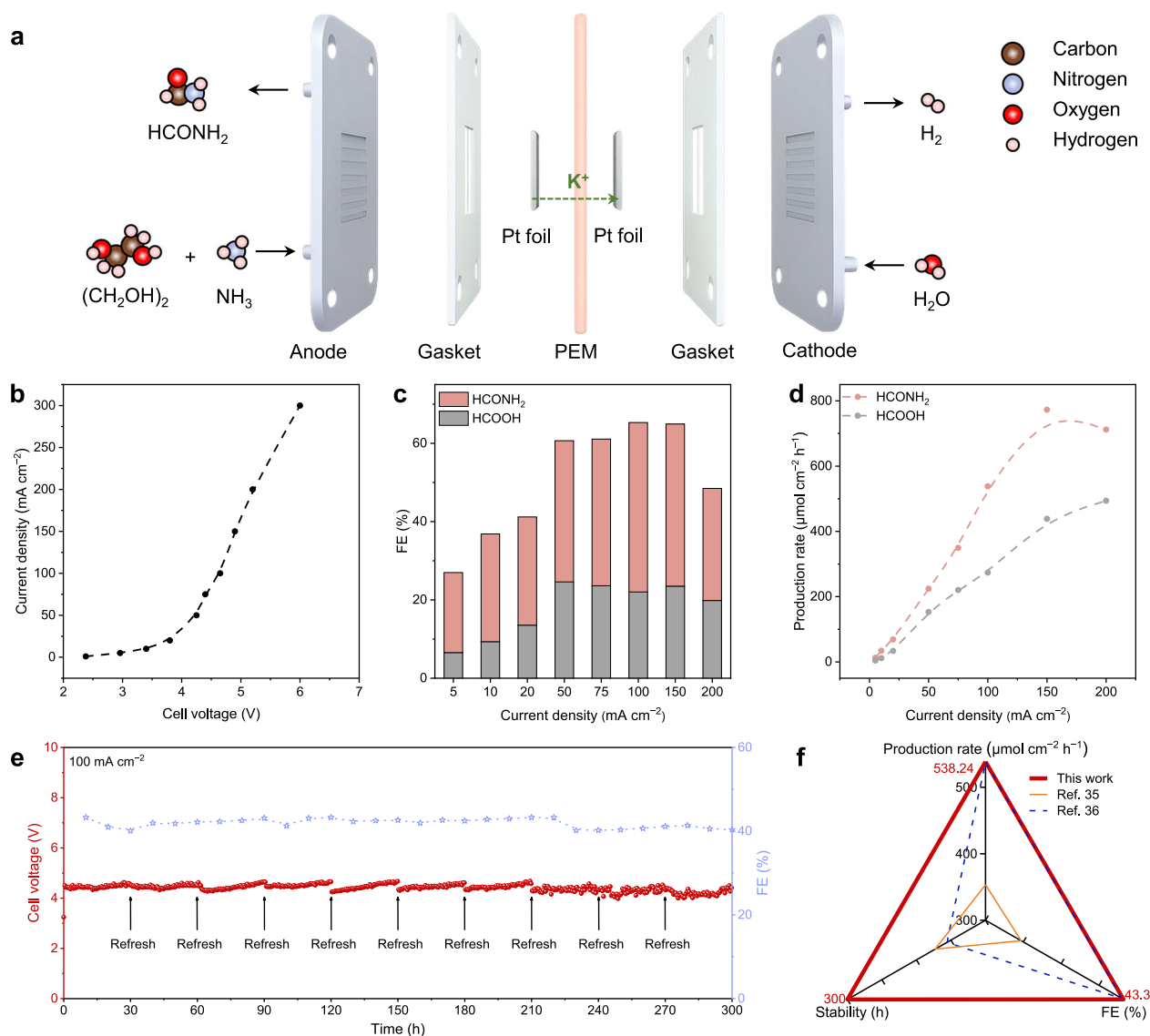
Fig. 5 | Continuous electrocatalytic production of HCONH₂. a Schematic of the MEA reactor using Pt foil electrodes separated by Nafion-117 for HCONH₂ synthesis through the co-oxidation reaction of EG and NH₃. **b** I−V curves (no iR compensation), (**c**) FEs, and (**d**) production rates of electrochemical HCONH₂ synthesis at different current densities. **e** Chronopotentiometry experiment profile showing the cell voltage (no iR compensation) and FEs of electrochemical HCONH₂ synthesis at 100 mA cm⁻² over 300 h in the MEA reactor (4.0 M EG + 1.0 M NH₃ + 0.5 M KHCO₃, electrolyte refreshed every 30 h. pH: 9.44 ± 0.032; Resistance: 3.87 ohms). **f** Radar plot comparing this work with other reported MEA-based systems. Source data are provided as a Source Data file.

cathode compartments are separated by a PEM (Nafion-117), which facilitates proton transport while maintaining the separation of the reactants. The effective geometric electrode area is restricted to 1.0 cm². The liquid flow rates on both the anode and cathode sides are maintained at 0.92 mL min⁻¹ using syringe pumps. The anode reaction continuously produces HCONH₂, while the cathode reaction generates hydrogen (H₂) gas (Fig. 5a), with a low impedance of 3.87 ohms during the reaction (Supplementary Fig. 32). This innovative design maintains a constant reactant concentration, simplifies the transport of reactants and the removal of products, and minimizes ohmic losses[67,68].

The I−V curve of the MEA system, covering the current density range of 1–300 mA cm⁻², is shown in Fig. 5b. The FE of HCONH₂ is changed in a pattern similar to that observed for the H-type cell, though it is slightly decreased, peaking at 43.3% at 100 mA cm⁻² and maintaining at 41.42% at 150 mA cm⁻² (Fig. 5c). The corresponding production rates are 538.42 μmol cm⁻²h⁻¹ and 772.8 μmol cm⁻²h⁻¹, respectively (Fig. 5d). It is worth noting that the FE of HCOOH for

the MEA system is higher than that for the H-type cell. Notably, the system maintains continuous and stable HCONH₂ production, sustaining an FE of approximately 40% for 300 h at 100 mA cm⁻² without significant fluctuations in the full-cell voltage, which remained around 4.65 V. (electrolyte refreshed every 30 hours, Fig. 5e). Such stability is essential to meet the requirements of industrial-scale production, since it ensures consistent output and reduces the need for frequent maintenance or adjustments on the systems. Notably, the radar plot underscores that the system possesses superior stability compared to the reported electrochemical systems for HCONH₂ production (Fig. 5f). Further performance comparisons, as provided in Supplementary Table 2, reveal that the system developed in this work for the electrosynthesis has substantial improvements in key metrics over other electrochemical synthesis methods. These enhancements demonstrate the distinct advantages of our MEA reactor design, including higher efficiency, reduced costs, and scalability for large-scale applications.
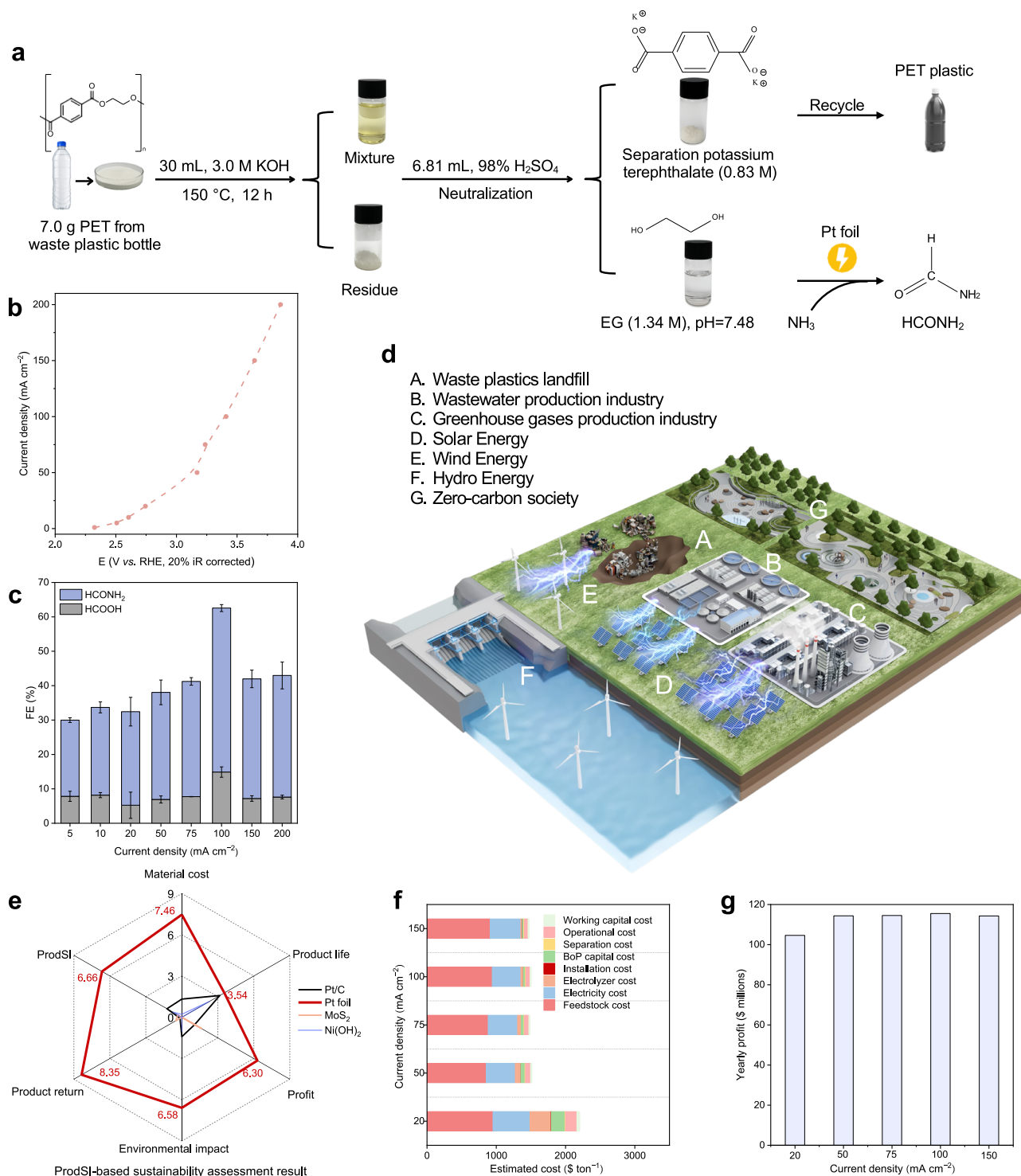
Fig. 6 | Evaluation of the electrochemical HCONH$_2$ production system from waste plastics. a Waste plastic upcycling process for HCONH$_2$ production. **b** I–V curves (with 20% iR compensation versus RHE), and (**c**) FEs of HCONH$_2$ synthesis at different current densities using EG derived from waste PET (1.34 M EG + 1.0 M NH$_3$ + 0.5 M KHCO$_3$. pH: 10.14 ± 0.02; Resistance: 6.541 ± 0.289 ohms). The error bars represent the standard deviation of three independent measurements. **d** Proposed integration of waste valorization into a circular energy system. **e** ProdSI-based sustainability assessment result of four catalysts. **f** Estimating production costs, and (**g**) projected yearly profits at different current densities. Source data are provided as a Source Data file.

Upcycling plastic waste to HCONH$_2$ as achieved at industrial-level current densities with ProdSI and TEA

Based on the successful conversion of EG and NH$_3$ into HCONH$_2$, the upcycling of wasted plastic bottles to HCONH$_2$ through the electrochemical synthesis route is implemented (Fig. 6a). As confirmed by the ^{1}H NMR spectra (Supplementary Figs. 33 and 34), EG and terephthalic acid (TPA) are the primary monomers produced during the initial step of PET depolymerization. TPA could be separated and recycled by the H$_2$SO$_4$ neutralization. The recovery and repurposing of TPA for the resynthesis of PET not only promotes a recycling economy but also adds value to the waste management process by creating a closed-loop system where materials are continuously reused. The step described

above ensures that the presence of TPA does not interfere with the efficiency of the subsequent electrochemical reactions.

Following the neutralization and separation processes, the resulting EG solution is co-oxidized with NH_3 to form $HCONH_2$. The electrochemical performance of the electrosynthesis system is evaluated, with the $I-V$ curve (with 20% iR compensation versus RHE) measured over a current density range of 1–200 mA cm^{-2}, as presented in Fig. 6b. The conversion ratio remains over 80%, indicating efficient utilization of reactants (Supplementary Fig. 35). The FE for $HCONH_2$ synthesis reaches $47.68 \pm 1.02\%$ at a current density of 100 mA cm^{-2} (Fig. 6c). At the higher current density of 200 mA cm^{-2}, a production rate of 879.4 ± 97.16 μmol cm^{-2} h^{-1} is obtained (Supplementary Fig. 36), highlighting the great potential of the system for high-throughput production and the scalability of the process. The proposed route not only facilitates the synthesis of valuable chemicals from plastic waste but also contributes to resolving the imminent environmental challenges posed by plastic waste. By combining the burgeoning renewable energy technologies, it is anticipated to generate more valuable materials from the wastes towards a net-zero society (Fig. 6d).

To this end, cost and sustainability evaluation are conducted using the ProdSI and TEA (Supplementary Note 1, and 2) methods to assess potential environmental and economic benefits. Akin to the depreciation of fixed assets, the cyclic decay rate exerts a strong impact on pragmatic employment, which is of equal importance to productivity and efficiency. Even tiny decay per cycle would be indefinitely magnified, especially at the industrial level. Under this occasion, the noble Pt foil is anticipated to afford low cost and better sustainability. An intuitionistic comparison in ProdSI is drawn between Pt foil and the other three catalysts, harnessing good initial performance. As illustrated in Fig. 6e, Pt foil catalyst demonstrates significant advantages over other catalyst counterparts among all sustainability considerations.

To further compare the advantages of Pt foil, we conduct two consecutive cycling tests on Pt/C, Pt foil, MoS_2 and $Ni(OH)_2$ catalysts in H-type cells at a current density of 100 mA cm^{-2}, and evaluated their cell voltage, FE and $HCONH_2$ generation rate (Supplementary Fig. 37). Pt foil exhibits stable performance, with negligible variation across cycles. In contrast, the other three catalysts show significant voltage decay, particularly in the second cycle, and a downward trend in both FE and yield. Notably, only Pt foil displays enhanced FE and productivity in the second cycle, which corresponds well with the increased surface O signal observed after long-term electrolysis (Supplementary Fig. 30), indicating a self-activation process involving the formation of Pt–O species. Importantly, this surficial oxidation does not lead to Pt loss, affirming the structural robustness of Pt foil under operating conditions.

We then conduct TEA on the synthesis of $HCONH_2$ over Pt foil. Detailed cost analysis shows that the plastic waste upcycling process can reduce the cost of $HCONH_2$ production to around $1500 per ton at a current density varying between 50 and 150 mA cm^{-2}, which is nearly $200 less than that of traditional methods (Fig. 6f). Moreover, the projected annual profit across different current densities remains relatively high and consistent, with an estimated profit of $115.50 million at a current density of 100 mA cm^{-2} (Fig. 6g). At current densities above 50 mA cm^{-2}, the estimated annual profit exceeds $114 million, suggesting promising applicability and industrial potential of our system for electrosynthesis. The net present value (NPV) analysis indicates that by the end of Year 3, the proposed factory will produce benefits, the cumulative present value will be over zero ($33.39 million). Over a 20-year operational period, the system is projected to generate a total profit exceeding $717.85 million under a current density of 100 mA cm^{-2}. These findings underscore the economic potential and environmental benefits of our upcycling approach for the production of $HCONH_2$ on a large scale, offering a sustainable and profitable solution for upcycling plastic waste to valuable products and tackling some imminent challenges in chemical synthesis.

Collectively, Pt foil catalyst, which might be labeled as 'high cost', should be qualified as a good catalyst in the scenario of $HCONH_2$ electrosynthesis. It is suggested that there should be a valuable comparison between the application of mature Pt foil processing technologies and the ongoing development of suitable nano-catalysts for catalytic electrosynthesis. Such concept could be extended to other unexplored industrial reactions (Supplementary Fig. 38).

Discussion

A sustainable and efficient strategy has been developed for the electrochemical synthesis of $HCONH_2$ via the co-oxidation of EG derived from PET waste and NH_3 over commercially Pt foil catalysts. Catalyst selection was guided by a combination of experimental screening and theoretical calculations. Employing $KHCO_3$ as the electrolyte establishes a mildly alkaline environment, which suppresses the formation of $(NH_4)_2SO_4$ by-products while preserving PET degradation efficiency. Under industrially relevant conditions, the system achieves an FE of $55.87 \pm 1.4\%$ and a production rate of 1003.63 ± 23.72 μmol cm^{-2} h^{-1}. Long-term electrolysis confirms operational durability, with stable performance maintained over more than 500 h and 300 h for the H-cell and MEA reactor, respectively. The reaction mechanism is proposed based on in situ ATR-SEIRAS, DEMS, and supported by DFT calculations. These analyzes suggest *CH_2O and *NH_2 as key surface-bound intermediates that promote $HCONH_2$ formation. Furthermore, TEA and ProdSI reveal that the use of noble metal catalysts, when properly evaluated, may offer competitive economic and environmental benefits compared to conventional energy-intensive processes. These findings provide a broader framework for reassessing the role of precious metal catalysts in sustainable electrosynthesis.

Methods
Chemicals and materials
Ethylene glycol ($C_2H_6O_2$, 99.5%, Aladdin), ammonia solution ($NH_3 \cdot H_2O$, 25-28%, Aladdin), potassium bicarbonate ($KHCO_3$, 99.5%, Aladdin), potassium hydroxide (KOH, 95%, Aladdin), potassium sulfate (K_2SO_4, 99%, Aladdin), sulfuric acid (H_2SO_4, 98%, RCI Labscan), formamide (CH_3NO, 99%, Aladdin), formic acid (CH_2O_2, 99%, Aladdin), polyethylene terephthalate (PET^{TM}CB-102, 300 mesh, Dupont), p-Phthalic acid ($C_8H_6O_4$, 99%, Aladdin), Nafion (5 wt.% in a mixture of lower aliphatic alcohols and water, contains 45% water, Aladdin), 2-proponal (C_3H_8O, Aladdin), deuterium oxide (D_2O, 99.9% atom% D, contains 0.05 wt% TMSP, Aladdin), dimethyl sulfoxide (C_2H_6OS, ≥ 99.9%, Sigma Aldrich) were used in the experiments. Platinum–ruthenium nanoparticles supported on carbon (PtRu/C), platinum nanoparticles supported on carbon (Pt/C), titanium dioxide (TiO_2), nickel hydroxide ($Ni(OH)_2$), nickel(II) oxide (NiO), cobalt(II,III) oxide (Co_3O_4), and silver (Ag) were purchased from Aladdin Company. Molybdenum disulfide (MoS_2) was obtained from Xianfeng Nano Company. Platinum (Pt) foil and palladium (Pd) foil were obtained from Shanghai Yueci Electronics Company. The DI water (18.25 MΩ·cm^{-1}) was used in all experiments.

Material characterizations
The morphologies of the samples were examined using a Hitachi SU-8230 field emission scanning electron microscope (FESEM). Operando Raman spectroscopy was conducted using a LabRAM HR800 Raman Spectroscopy System (Supplementary Fig. 39a). In situ attenuated total reflectance surface-enhanced infrared absorption spectroscopy (ATR-SEIRAS) measurements were conducted using a BRUKER Invenio Fourier-transform infrared (FTIR) spectrometer equipped with a diamond ATR window (Supplementary Fig. 39b). Spectra were collected in ATR-SEIRAS mode with 64 scans and a spectral resolution better than 4 cm^{-1}. X-ray photoelectron spectroscopy (XPS) was conducted on a Kratos AXIS UltraDLD with Al-Kα radiation (1486 eV) to gain the chemical composition and state of samples. X-ray diffraction (XRD) analysis was performed using a Rigaku Smart Lab 9 kW X-ray Diffractometer.

In situ differential electrochemical mass spectrometry (DEMS) measurements

In situ DEMS measurements were performed using an HPR-40 quadrupole mass spectrometer (Hiden Analytical, UK) equipped with a gas-permeable PTFE membrane inlet (thickness: 60 μm, pore size: 0.22 μm, porosity: 50%). The catalyst ink was drop-cast onto the PTFE membrane, which served as the working electrode. A saturated calomel electrode (Hg/Hg$_2$Cl$_2$) and a Pt wire were used as the reference and counter electrodes, respectively (Supplementary Fig. 39c). The electrolyte consisted of 4.0 M EG, 1.0 M NH$_3$, and 0.5 M KHCO$_3$ in aqueous solution.

Prior to electrolysis, the system was stabilized under open-circuit conditions for 30 min to establish the baseline signal. Subsequently, alternating potential cycling was applied between 1.2 V and 2.8 V vs Hg/Hg$_2$Cl$_2$ for 6 consecutive cycles, lasting a total of 3000 s. During the entire process, the mass spectrometer continuously monitored the gaseous products in real-time. The characteristic mass-to-charge (m/z) ratios of 46 (H$_2$NCHO), 45 (HCONH$_2$), 30 (CH$_2$O), and 16 (NH$_2$) were tracked, and the corresponding signal intensities were baseline-corrected using the open-circuit background. No isotope labeling was used in this study.

Preparation of electrodes

For Pt foil and Pd foil experiments, commercial Pt foil and Pd foil (99.99%, 1.0 cm^2, 0.1 mm thickness) were used directly as the working electrode after ultrasonic cleaning in ethanol and deionized water for 5 min each.

For all other catalysts were prepared as follows: 40 mg of catalyst powder was dispersed in 4.0 mL of isopropanol (Aladdin) and 160 μL of Nafion solution (Aladdin). The ink was ultrasonicated in an ice-water bath for 30 min to ensure homogeneity, and then airbrushed onto a 5 × 5 cm^2 hydrophilic carbon paper (TGP-H060H(M), Toray, purchased via Science Materials Station). The resulting electrode was dried under vacuum at room temperature (20 °C) for 24 h before use with a geometric area of 1.0 cm^2.

Activation of the Nafion-117 membrane

The proton exchange membrane (PEM, Nafion-117) was purchased from Fuel Cell Store. It was pretreated in 5% H$_2$O$_2$ and 10% H$_2$SO$_4$ solutions at 80 °C for 1 h each before use. The membrane thickness is ~183 μm, and the size was cut to match a 1.0 cm^2 active area.

Electrochemical measurements

All electrochemical measurements were conducted on a BioLogic VSP-300 electrochemical workstation at room temperature (20 °C). All data were collected with EC-Lab software, and post-processing was performed using Origin.

Electrochemical measurements were conducted in a dual-chamber H-type electrolytic cell (C007-10, Gaoss Union) with each compartment containing 10.0 mL of electrolyte. A three-electrode configuration was used, with Pt foil acting as the counter and reference electrodes. We used a three-electrode configuration in an H-type cell, with Pt foil acting as the counter and reference electrodes. For all the reactions, Hg/Hg$_2$Cl$_2$ were used as reference electrodes. All potentials measured were calibrated to the reversible hydrogen electrode (RHE) by the Eq. (1):

$$E_{RHE} = E_{Hg/Hg_2Cl_2} + 0.0591 \times pH + 0.2412 \qquad (1)$$

The Hg/Hg$_2$Cl$_2$ reference electrode was calibrated against a reversible hydrogen electrode (RHE) in 0.5 M H$_2$SO$_4$ by recording the hydrogen evolution/oxidation potential on a Pt black electrode under continuous H$_2$ purging. The zero-current potential was identified as 0 V vs. RHE, allowing us to determine the offset potential of the reference electrode. The reference electrode was calibrated regularly to ensure accuracy. All potentials in the manuscript have been converted

accordingly. The compartments were separated by a proton exchange membrane (PEM, Nafion-117 purchased from Fuel Cell Store).

Electrochemical impedance spectroscopy measurements were carried out in a frequency range of 0.01-100,000 Hz with an amplitude of 6.0 mV. The uncompensated cell resistance was measured via EIS before each experiment. Linear sweep voltammetry and cyclic voltammetry of anodic reactions was measured at a scan rate of 5.0 mV s^{-1}. The electrolyte solution consisting of 4.0 M EG, 1.0 M NH$_3$, and 0.5 M KHCO$_3$ was freshly prepared before each experiment. For 500 mL of electrolyte: Ethylene glycol (C$_2$H$_6$O$_2$, 99.5%, Aladdin): 111.5 mL, ammonia solution (NH$_3$.H$_2$O, 25-28%, Aladdin): 34.08 mL, potassium bicarbonate (KHCO$_3$, 99.5%, Aladdin): 25.03 g. These components were sequentially added into deionized water under continuous magnetic stirring until fully dissolved. The mixture was then diluted to 500 mL with deionized water. The electrolyte was used immediately or stored in a sealed container at room temperature (20 °C) for no more than 24 h. The pH of the electrolyte (4.0 M EG + 1.0 M NH$_3$ + 0.5 M KHCO$_3$) was also measured at room temperature (20 °C) using a calibrated pH meter, yielding a value of 9.44 ± 0.032 ($n = 3$)

Membrane electrode assembly (MEA) reactor

The Pt foil electrode was used as the anode and cathode for formamide synthesis. The two electrodes were positioned on opposite sides and separated by a proton exchange membrane (PEM, Nafion-117 purchased from Fuel Cell Store). The geometric surface area of the catalyst is 1.0 cm^2. On the cathode side, a stainless-steel gas flow chamber supplied DI water while the anode was supply with 4.0 M EG + 1.0 M NH$_3$ + 0.5 M KHCO$_3$. The flow rate was 0.92 ml min^{-1} in both chambers, controlled by a syringe pump. Impedance (IR) compensation was not performed unless specifically stated. The MEA device maintains continuous and stable HCONH$_2$ production, sustaining an FE of approximately 40% for 300 hours at 100 mA cm^{-2} without significant fluctuations in the full-cell voltage, which remained around 4.65 V (electrolyte refreshed every 30 hours).

Product analysis

One-dimensional ^{1}H NMR spectra were collected on a JEOL ECZ500R 500 MHz Solid-State nuclear magnetic resonance (NMR) spectrometer to quantify the liquid products at the anode. Typically, 500 μl of the electrolyte after electrolysis was mixed with 49.0 μl of D$_2$O (Aladdin, 99.9 at% D) and 1.0 μl dimethyl sulfoxide (Sigma Aldrich, ≥ 99.9%) as internal standard. Gas products were analyzed online using an Agilent 7890B gas chromatograph (GC) equipped with a high-sensitivity flame ionization detector (FID) and a thermal conductivity detector (TCD). The FID was used for hydrocarbons and other carbon-containing organics, while the TCD provided a strong response for inorganic gases (e.g., O$_2$ and N$_2$). High-purity helium served as the carrier gas at 1.0 mL product identities and concentrations were determined by min^{-1}. Comparison with certified gas standards. The detected gas were O$_2$, CO$_2$, CO, N$_2$, NO, and NO$_2$.

The corresponding FE was calculated as Eq. (2):

$$FE = \frac{CV*F*n_i}{It}, \qquad (2)$$

where n_i is the number of electrons transferred in one product molecule, whereas the value is 3 for formamide and 4 for formic acid formation, respectively. F is the Faraday constant (96485 C mol^{-1}); C is the concentration of the formamide and formic acid calculated by the calibration curve, and V is the volume of the electrolyte.

The production rate and conversion ratio were calculated based on the Eq. (3)−(4):

$$Production\ rate = \frac{CV}{t}, \qquad (3)$$

$$\text{Conversion ratio} = \frac{\text{weight of the the target products}}{\text{weight of the inlet fed into the reactor}}. \quad (4)$$

Data availability

The data generated in this study are provided in the Supplementary Information and Source Data file. All data supporting the findings of this study are available within the paper and its Supplementary Information or from the corresponding authors upon request. Source data are provided in this paper.

Code availability

The central code used in this paper is VASP. Detailed information related to the license and user guide are available at https://www.vasp.at. Other codes used in the study are available from the corresponding authors upon request.

References

1. Yang, H. et al. Amine-impregnated polymeric resin with high CO_2 adsorption capacity for biogas upgrading. *Chem. Eng. J.* **430**, https://doi.org/10.1016/j.cej.2021.132899 (2022).
2. Xia, Q. et al. Efficient synthesis of organosulfur compounds via electrochemical biomass conversion. *Nat. Synth.* **4**, 765–775 (2025).
3. Tang, M. et al. High-energy-density aqueous zinc-ion batteries: recent progress, design strategies, challenges, and perspectives. *Adv. Mater.* e2501361 https://doi.org/10.1002/adma.202501361 (2025).
4. Zou, X. et al. Carbon-based electrocatalysts for rechargeable Zn-air batteries: design concepts, recent progress and future perspectives. *Energy Environ. Sci.* **17**, 386–424 (2024).
5. Wu, J. et al. Immobilizing ordered oxophilic indium sites on platinum enabling efficient hydrogen oxidation in alkaline electrolyte. *J. Am. Chem. Soc.* **146**, 20323–20332 (2024).
6. Zhu, P. et al. Continuous carbon capture in an electrochemical solid-electrolyte reactor. *Nature* **618**, 959–966 (2023).
7. Chen, F. Y. et al. Efficient conversion of low-concentration nitrate sources into ammonia on a Ru-dispersed Cu nanowire electrocatalyst. *Nat. Nanotechnol.* **17**, 759–767 (2022).
8. Li, Y. et al. Sequential co-reduction of nitrate and carbon dioxide enables selective urea electrosynthesis. *Nat. Commun.* **15**, 176 (2024).
9. Gong, S. et al. Paired electrolysis for efficient coproduction of CO and S8 with techno-economic analysis. *Chem. Eng. J.* **507**, 160286 (2025).
10. Wang, X. et al. Reaction and reactor designs for improving electrochemical CO_2 capture. *Device* **3**, 100837 (2025).
11. Corma, A. Heterogeneous catalysis: Understanding for designing, and designing for applications. *Angew. Chem. Int. Ed. Engl.* **55**, 6112–6113 (2016).
12. Trindell, J. A., Duan, Z., Henkelman, G. & Crooks, R. M. Well-defined nanoparticle electrocatalysts for the refinement of theory. *Chem. Rev.* **120**, 814–850 (2020).
13. Zhang, Y. et al. Design and regulation of defective electrocatalysts. *Chem. Soc. Rev.* **53**, 10620–10659 (2024).
14. Peljo, P. & Kallio, T. Electrocatalyst nanoparticles go with the flow. *Nat. Catal.* **4**, 445–446 (2021).
15. Sun, L., Reddu, V. & Wang, X. Multi-atom cluster catalysts for efficient electrocatalysis. *Chem. Soc. Rev.* **51**, 8923–8956 (2022).
16. Duchesne, P. N. et al. Golden single-atomic-site platinum electrocatalysts. *Nat. Mater.* **17**, 1033–1039 (2018).
17. Xu, H., Cheng, D., Cao, D. & Zeng, X. C. A universal principle for a rational design of single-atom electrocatalysts. *Nat. Catal.* **1**, 339–348 (2018).
18. Minguzzi, A. How to improve the lifetime of an electrocatalyst. *Nat. Catal.* **3**, 687–689 (2020).
19. Sorsa, O. et al. Optimization and aging of Pt nanowires supported on single-walled carbon nanotubes as a cathode catalyst in polymer electrolyte membrane water electrolyser. *Int. J. Hydrog. Energy* **45**, 19121–19132 (2020).
20. Liu, L. & Corma, A. Structural transformations of solid electrocatalysts and photocatalysts. *Nat. Rev. Chem.* **5**, 256–276 (2021).
21. Akbashev, A. R. Electrocatalysis goes nuts. *ACS Catal.* **12**, 4296–4301 (2022).
22. Xie, C., Chen, W., Wang, Y., Yang, Y. & Wang, S. Dynamic evolution processes in electrocatalysis: structure evolution, characterization and regulation. *Chem. Soc. Rev.* **53**, 10852–10877 (2024).
23. Beyazay, T., Martin, W. F. & Tuysuz, H. Direct synthesis of formamide from CO_2 and H_2O with nickel-iron nitride heterostructures under mild hydrothermal conditions. *J. Am. Chem. Soc.* **145**, 19768–19779 (2023).
24. Massolo, E., Pirola, M. & Benaglia, M. Amide bond formation strategies: Latest advances on a dateless transformation. *Eur. J. Org. Chem.* **2020**, 4641–4651 (2020).
25. Guo, C. et al. Electrochemical upgrading of formic acid to formamide via coupling nitrite co-reduction. *J. Am. Chem. Soc.* **144**, 16006–16011 (2022).
26. Lu, Y. et al. Anodic electrosynthesis of amide from alcohol and ammonia. *CCS Chem.* **6**, 125–136 (2024).
27. Lan, J. et al. Efficient electrosynthesis of formamide from carbon monoxide and nitrite on a Ru-dispersed Cu nanocluster catalyst. *Nat. Commun.* **14**, 2870 (2023).
28. Ramadhany, P. et al. Triggering C–N coupling on metal oxide nanocomposite for the electrochemical reduction of CO_2 and NO_x^- to formamide. *Adv. Energy Mater.* **14**, 2401786 (2024).
29. Meng, N. et al. Electrosynthesis of formamide from methanol and ammonia under ambient conditions. *Nat. Commun.* **13**, 5452 (2022).
30. Yang, W. et al. Photocatalytic formamide synthesis via coupling of electrophilic and nucleophilic radicals over atomically dispersed Bi sites. *Angew. Chem. Int. Ed. Engl.* **63**, e202408379 (2024).
31. Mou, S., Liu, S., Dai, W., Sun, Y. & Dong, F. Fluorine-induced D-band center shift in Nb_2O_5 nanosheets for efficient electrochemical formamide synthesis. *Appl. Catal. B Environ.* **365**, 124963 (2025).
32. Shi, Q. et al. Electrocatalytic upgrading of plastic and biomass-derived polyols to formamide under ambient conditions. *Angew. Chem., Int. Ed. Engl.* **63**, e202407580 (2024).
33. Li, X. Y., Zhang, Z. M., Zhuang, X. X., Jia, Z. T. & Wang, T. Electrolyte effects in electrocatalytic kinetics. *Chin. J. Chem.* **42**, 3533–3552 (2024).
34. Yan, Y. et al. Electrocatalytic upcycling of biomass and plastic wastes to biodegradable polymer monomers and hydrogen fuel at high current densities. *J. Am. Chem. Soc.* **145**, 6144–6155 (2023).
35. Zhou, H. et al. Electrocatalytic upcycling of polyethylene terephthalate to commodity chemicals and H_2 fuel. *Nat. Commun.* **12**, 4679 (2021).
36. Abedsoltan, H. A focused review on recycling and hydrolysis techniques of polyethylene terephthalate. *Polym. Eng. Sci.* **63**, 2651–2674 (2023).
37. Yu, H. et al. Biobased dimethyl isosorbide as an efficient solvent for alkaline hydrolysis of waste polyethylene terephthalate to terephthalic acid. *Green. Chem.* **25**, 7807–7816 (2023).
38. Chen, J. et al. Accelerating discovery of next-generation power electronics materials via high-throughput ab initio screening. *Npj Comput. Mater.* **11**, 249 (2025).
39. Lin, X.-M. et al. In situ probe of the hydrogen oxidation reaction intermediates on PtRu a bimetallic catalyst surface by core-shell nanoparticle-enhanced Raman spectroscopy. *Nano Lett.* **22**, 5544–5552 (2022).
40. Huang, Y. F., Kooyman, P. J. & Koper, M. T. Intermediate stages of electrochemical oxidation of single-crystalline platinum revealed by in situ Raman spectroscopy. *Nat. Commun.* **7**, 12440 (2016).

41. Wang, Z. et al. Ultrafine PtO_2 nanoparticles coupled with a Co(OH)F nanowire array for enhanced hydrogen evolution. *Chem. Commun.* **54**, 810–813 (2018).

42. Sun, Y. L. et al. Visualization of electrooxidation on palladium single crystal surfaces via in situ Raman spectroscopy. *Angew. Chem. Int. Ed. Engl.* **63**, e202408736 (2024).

43. Louie, M. W. & Bell, A. T. An investigation of thin-film Ni-Fe oxide catalysts for the electrochemical evolution of oxygen. *J. Am. Chem. Soc.* **135**, 12329–12337 (2013).

44. Joya, K. S. & Sala, X. In situ Raman and surface-enhanced Raman spectroscopy on working electrodes: spectroelectrochemical characterization of water oxidation electrocatalysts. *Phys. Chem. Chem. Phys.* **17**, 21094–21103 (2015).

45. Huang, J. et al. In situ monitoring of the electrochemically induced phase transition of thermodynamically metastable 1T-MoS_2 at nanoscale. *Nanoscale* **12**, 9246–9254 (2020).

46. Doan, T. L., Nguyen, T. N., Hong, H. & Kim, T. Development of an oxygen evolution reaction electrocatalyst of TiO_2 supported IrO_2 (IrO_2@TiO_2) for enhancing performance and durability of polymer electrolyte membrane water electrolysis. *Int. J. Hydrog. Energy* **110**, 754–763 (2024).

47. Luo, H., Ji, X. & Cheng, S. Investigation into the electrochemical behaviour of silver in alkaline solution and the influence of Au-decoration using operando Raman spectroscopy. *RSC Adv.* **10**, 8453–8459 (2020).

48. Iriawan, H. et al. Methods for nitrogen activation by reduction and oxidation. *Nat. Rev. Methods Prim.* **1**, 1–26 (2021).

49. Dann, E. K. et al. Structural selectivity of supported Pd nanoparticles for catalytic NH_3 oxidation resolved using combined operando spectroscopy. *Nat. Catal.* **2**, 157–163 (2019).

50. Pignet, T. & Schmidt, L. Kinetics of NH_3 oxidation on Pt, Rh, and Pd. *J. Catal.* **40**, 212–225 (1975).

51. Hong, W., Shang, C., Wang, J. & Wang, E. Bimetallic PdPt nanowire networks with enhanced electrocatalytic activity for ethylene glycol and glycerol oxidation. *Energy Environ. Sci.* **8**, 2910–2915 (2015).

52. Yue, H., Zhao, Y., Ma, X. & Gong, J. Ethylene glycol: properties, synthesis, and applications. *Chem. Soc. Rev.* **41**, 4218–4244 (2012).

53. Xin, L., Zhang, Z., Qi, J., Chadderdon, D. & Li, W. Electrocatalytic oxidation of ethylene glycol (EG) on supported Pt and Au catalysts in alkaline media: Reaction pathway investigation in three-electrode cell and fuel cell reactors. *Appl. Catal. B* **125**, 85–94 (2012).

54. Kang, H. et al. Mining the carbon intermediates in plastic waste upcycling for constructing C-S bond. *J. Am. Chem. Soc.* **146**, 18639–18649 (2024).

55. Gunanathan, C., Ben-David, Y. & Milstein, D. Direct synthesis of amides from alcohols and amines with liberation of H_2. *Science* **317**, 790–792 (2007).

56. Yamaguchi, K., Kobayashi, H., Oishi, T. & Mizuno, N. Heterogeneously catalyzed synthesis of primary amides directly from primary alcohols and aqueous ammonia. *Angew. Chem. Int. Ed. Engl.* **51**, 544–547 (2011).

57. Gong, L. et al. Recent development of methanol electrooxidation catalysts for direct methanol fuel cell. *J. Energy Chem.* **27**, 1618–1628 (2018).

58. Nagaraj, R. et al. Fructose and methylglyoxal-induced glycation alters structural and functional properties of salivary proteins, albumin and lysozyme. *Plos ONE* **17**, e0262369 (2022).

59. Li, X. et al. Photocatalytic C–N coupling from stable and transient intermediates for gram-scale acetamide synthesis. *Nat. Commun.* **16**, 3590 (2025).

60. McNaughton, D., Evans, C. J., Lane, S. & Nielsen, C. J. The high-resolution FTIR far-infrared spectrum of formamide. *J. Mol. Spectrosc.* **193**, 104–117 (1999).

61. Sugawara, Y., Hamada, Y. & Tsuboi, M. Vibration-rotation spectra of formamides. *Bull. Chem. Soc. Jpn.* **56**, 1045–1050 (1983).

62. Brummel, C. L., Shen, M., Hewett, K. B. & Philips, L. A. High-resolution infrared spectroscopy of formamide and deuterated formamide in a molecular beam. *J. Opt. Soc. Am. B* **11**, 176–183 (1994).

63. Shi, Y. et al. Unveiling hydrocerussite as an electrochemically stable active phase for efficient carbon dioxide electroreduction to formate. *Nat. Commun.* **11**, 3415 (2020).

64. Xia, Q. et al. Methanol-facilitated surface reconstruction catalysts for near 200% faradaic efficiency in a coupled system. *Adv. Funct. Mater.* **34**, 2314596 (2024).

65. Bavarella, S. et al. Chemically reactive membrane crystallisation reactor for CO_2–NH_3 absorption and ammonium bicarbonate crystallisation: Kinetics of heterogeneous crystal growth. *J. Membr. Sci.* **599**, 117682 (2020).

66. Leaist, D. Proton-coupled transport of ammonia in aqueous hydrochloric acid. *Aust. J. Chem.* **38**, 249–260 (1985).

67. Xu, Q. et al. Identifying and alleviating the durability challenges in membrane-electrode-assembly devices for high-rate CO electrolysis. *Nat. Catal.* **6**, 1042–1051 (2023).

68. Wan, L. et al. Oriented intergrowth of the catalyst layer in membrane electrode assembly for alkaline water electrolysis. *Nat. Commun.* **13**, 7956 (2022).

Acknowledgements

Author contributions

X.Z.W., G.P.Z., S.X.D., X.Z., and J.Y.S. conceived the idea. X.Z.W. designed the experiments, performed the electrochemical tests, and explored the mechanisms. J.S.C., X.Z.W., and Y.W.S. contributed to the theoretical calculation. X.Z.W., E.H.Y., and W.S.Y. calculated the ProdSI and TEA of this study. X.Z.Y. assisted in gas product tests. Y.Y.Y., J.J.W., and F.J.X. assisted in SEM. X.Z.W. wrote the paper. X.Z.W., Y.W.S., M.C.T., Y.B.M., Q.X., J.W., and S.H.G. revised the manuscript. All authors discussed the results and commented on the manuscript.

Competing interests

The authors declare no competing interests

Additional information